Mesoscopic model for filament orientation in growing actin networks: the role of obstacle

geometry

Mesoscopic model for filament orientation in growing actin networks: the role of obstacle geometry

Julian Weichsel[1,2] **and Ulrich S Schwarz**[1]

[1] Bioquant and Institute for Theoretical Physics, University of Heidelberg, Heidelberg, Germany
[2] Department of Chemistry, University of California at Berkeley, CA, USA
E-mail: weichsel@berkeley.edu
and ulrich.schwarz@bioquant.uni-heidelberg.de

Abstract. Propulsion by growing actin networks is a universal mechanism used in many different biological systems, ranging from the sheet-like lamellipodium of crawling animal cells to the actin comet tails induced by certain bacteria and viruses in order to move within their host cells. Although the core molecular machinery for actin network growth is well preserved in all of these cases, the geometry of the propelled obstacle varies considerably. During recent years, filament orientation distribution has emerged as an important observable characterizing the structure and dynamical state of the growing network. Here we derive several continuum equations for the orientation distribution of filaments growing behind stiff obstacles of various shapes and validate the predicted steady state orientation patterns by stochastic computer simulations based on discrete filaments. We use an ordinary differential equation approach to demonstrate that for flat obstacles of finite size, two fundamentally different orientation patterns peaked at either $\pm 35°$ or $+70°/0°/-70°$ exhibit mutually exclusive stability, in agreement with earlier results for flat obstacles of very large lateral extension. We calculate and validate phase diagrams as a function of model parameters and show how this approach can be extended to obstacles with piecewise straight contours. For curved obstacles, we arrive at a partial differential equation in the continuum limit, which again is in good agreement with the computer

IOP Institute of Physics ⦿ DEUTSCHE PHYSIKALISCHE GESELLSCHAFT

simulations. In all cases, we can identify the same two fundamentally different orientation patterns, but only within an appropriate reference frame, which is adjusted to the local orientation of the obstacle contour. Our results suggest that two fundamentally different network architectures compete with each other in growing actin networks, irrespective of obstacle geometry, and clarify how simulated and electron tomography data have to be analyzed for non-flat obstacle geometries.

Contents

1. Introduction

The growth of actin networks is a generic propulsion mechanism occurring in a large variety of biological systems, ranging from the protruding lamellipodia of animal cells to the actin comet tails recruited by pathogens like the bacterium *Listeria monocytogenes* or the virus *Vaccinia* within their host cells. Due to its central importance, the molecular basis of this process is well preserved over a wide range of different species [1]. Although a large number of accessory proteins is known to be involved in actin dynamics on the cellular scale, in regions close to the leading edge the dynamics of network growth are determined by a small number of key reactions. Here the interplay between three fundamental processes determines the structure of the growing network: polymerization of filamentous actin, branching mediated by the protein complex Arp2/3 and binding of capping proteins to the filament tip preventing further growth [2, 3]. The fact that these processes are highly conserved is impressively demonstrated by the observation that many intracellular pathogens rely on them for efficient infection and spread in the cytoplasm of their hosts [4–6]. Even functionalized plastic beads, rods and discs as well as lipid vesicles and oil droplet in purified protein solutions containing this minimal set of molecules have been shown to be propelled *in vitro* by polymerizing actin networks [7–12].

While the underlying molecular basis is very similar in all of these cases, the geometry of the different propelled objects is very different. For instance, the highly curved shape of relatively small, almost ellipsoidal pathogens like *Listeria monocytogenes* or *Vaccinia* virus is very different from the relatively flat shape of the leading edge of a crawling cells. The exact

shape of the membrane in migrating cells is very dynamic, but certainly corrugated on different scales, thus in this case a flat obstacle shape can only be a first approximation and corrugated obstacle contours are also of large interest. In a growing actin network, new filaments nucleate by branching off from existing mother filaments at a characteristic angle around $70°$ set by the molecular geometry of the Arp2/3-complex. Importantly, branching can occur only close to the surface, as it depends on the presence of surface-bound nucleation promoting factors (NPFs) like Wiskott–Aldrich syndrome protein (WASP) or ActA [13]. Whether the daughter filament becomes a productive member of the growing actin gel depends on the way its direction is oriented relative to the direction of growth and how the object is shaped. Therefore obstacle geometry is a crucial determinant of the resulting structural organization of the network.

One essential function of growing actin networks is to generate force against external load. Force–velocity relations for growing actin networks have been measured in different experimental setups and for various obstacle shapes [14–20]. Unexpected discrepancies in the results indicate that obstacle shape and the resulting difference in network organization also has an effect on force generation. Modern electron tomography leads to visualization and analysis of filamentous actin networks in ever greater detail [21, 22]. While early electron microscopy (EM) data for the lamellipodia of fish keratocytes suggested a dendritic network of relatively short actin filaments [23], recent electron tomography data has revealed a more diverse structural organization, with relatively long filaments connected by few branch points into different and spatially extended filament subsets [22, 24]. In addition, it has been demonstrated that the structural organization of the network strongly depends on the protrusion speed, with fast growing networks dominated by two symmetric diagonal filament orientations and slowly growing networks featuring more filaments in parallel and orthogonal to the leading edge [25, 26]. It is to be expected, that in the future the effect of obstacle geometry on network structure can be quantified by such methods as well.

In order to achieve a complete understanding of the structure of growing actin networks, different modeling approaches have been developed during the last decade [27], ranging from microscopic ratchet models [28, 29], rate equations for filament growth [30–32] and large-scale computer simulations of filament ensembles [33–36] to continuum theories of how elastic stress propels the obstacle [37] and multi-scale models combining several of these model classes [20, 38]. From some of these studies it has emerged that one central quantity characterizing the structural organization of growing actin networks is the filament orientation distribution, which can be directly compared with experimental results [26, 31, 39, 40].

In the following, we study a model which allows us to predict the filament orientation distribution as a function of obstacle geometry. Our reference point will be stochastic computer simulations of growing actin networks incorporating the molecular processes of branching, capping and filament polymerization [32]. For computational simplicity and deeper insight, these will be compared to different versions of a rate equation model [30–32]. For actin growth behind flat and laterally widely spread obstacles the steady state organization has been predicted earlier to be either a $±35°$ or $+70°/0°/-70°$ filament orientation pattern, with mutually exclusive stability determined by the model parameters [31, 32]. In this paper, we will extend this analysis to also predict the effect of finite size and geometry of the propelled object. In particular, we will derive and validate a partial differential equation (PDE), which is valid also for curved obstacle shapes.

The paper is organized as follows. In section 2 we introduce the model and explain how we analyze it. To validate our results, we compare different versions of a deterministic continuum
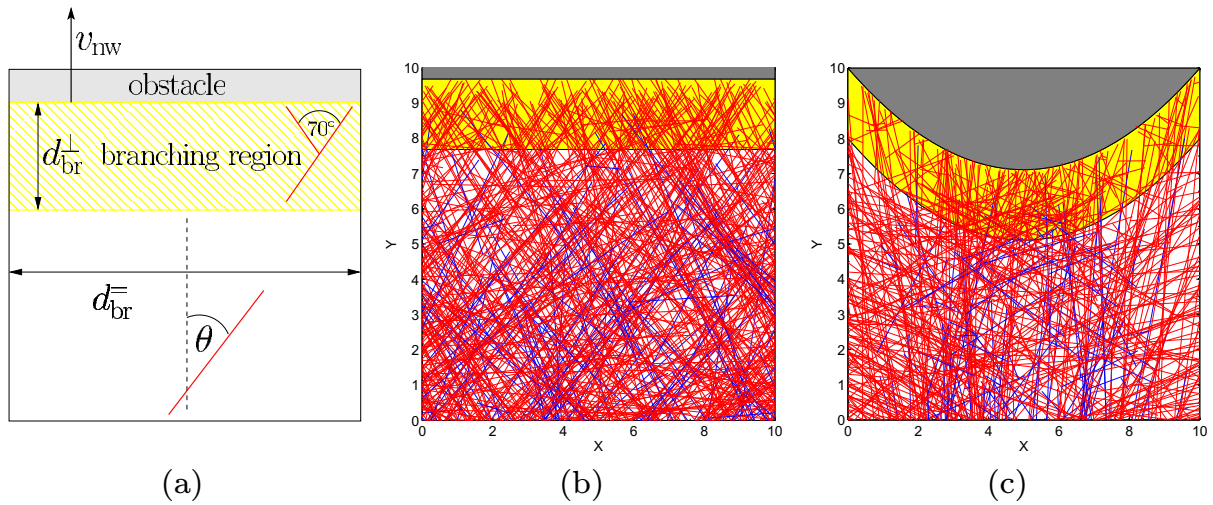
Figure 1. Model of a growing actin network behind a rigid obstacle. (a) Sketch of the setup. Branching can occur only in the yellow region. The main quantity of interest is the filament orientation angle θ relative to the surface normal. (b) Snapshot of a stochastic simulation based on the reactions of individual filaments for straight (*linear*) obstacle shape. (c) Snapshot of network growth behind a curved (*nonlinear*) obstacle shape. The network is growing in two dimensions. Red filaments are actively growing at their barbed end in direction θ. Blue filaments have been capped and will eventually be outgrown by the network and leave the box at the bottom. Growth of the fastest filaments is stalled by the obstacle.

model to stochastic computer simulations of filamentous networks. Subsequently, the impact of different piecewise straight (*linear*) obstacle shapes on the resulting network orientation patterns is analyzed in section 3, while specific examples for curved (*nonlinear*) obstacle shapes are the subject of section 4. Our main result is that the competition between two fundamentally different network architectures persists for finite-sized, piecewise linear and curved obstacles.

2. Model definition

Motivated by established biological observations, in our model we assume Arp2/3 to nucleate daughter filaments from preexisting mother filaments at a characteristic relative branching angle around $70°$ [2, 23, 41]. The exact value varies with biological system and analysis methods (e.g. a recent value from electron tomography data for the lamellipodium of fibroblasts is $73 \pm 8°$ [22]), but is not essential for our theory. Although the exact mechanism for the activation of Arp2/3-mediated branching is not yet well established and subject of current research, it is generally accepted that Arp2/3 is active only near the obstacle, where it is activated by NPFs such as the WASP or the bacterial actin assembly-inducing protein (ActA) [13, 42, 43]. As we are interested in actin network architecture in close proximity to the surface of a propelled obstacle, we will focus on actin dynamics within the first few ten nanometers from the obstacle surface in which filament branching, capping and barbed end polymerization are expected to dominate actin dynamics, while filament depolymerization and decapping can be neglected [44]. Figure 1(a) sketches the geometrical arrangement studied here. The yellow *branching region*

within a vertical distance $d_{\mathrm{br}}^{\perp}$ from the obstacle surface indicates the domain in which filament bound Arp2/3 is able to interact with NPFs, which themselves are active only close to the surface. Thus filament branching occurs in this branching region. Once filament barbed ends have left this domain due to their retrograde flow they are not able to nucleate new daughter filaments anymore and will eventually be outgrown by the bulk network. As those filaments subsequently do not impact the orientation distribution at the leading edge, we do not explicitly account for their further fate anymore. If the lateral extension $d_{\mathrm{br}}^{=}$ of the obstacle is large compared to the width $d_{\mathrm{br}}^{\perp}$ of the branching region, it is possible to neglect the process of filament barbed ends growing out of the branching region horizontally. However, for relatively small obstacles, for instance viral pathogens, the lateral dimension of the propelled particle $d_{\mathrm{br}}^{=}$ can become comparable to its vertical extension $d_{\mathrm{br}}^{\perp}$ and the finite lateral size of the branching region has to be taken into account. Our main quantity of interest is the filament orientation angle θ relative to the surface normal.

In the following, we will validate our theoretical approach by comparing results from two complementary implementations, namely stochastic computer simulations and a rate equation approach, which have been introduced before for flat obstacles of large lateral size [32]. Motivated by the flat nature of the lamellipodium and also for computational simplicity, our modeling is restricted to two dimensions. Representative snapshots of such simulations for flat and curved obstacle geometries are given in figures 1(b) and (c), respectively. Briefly, we simulate a network of infinitely stiff rods. This simplification is justified as the reaction kinetics that eventually determine the stable orientation distribution in steady state are active within a narrow branching region along the obstacle only. Because filament segments spanning over this region are very short compared to their persistence length (nanometers versus micrometers), local bending undulations are of minor importance here. The remainder of the filaments is considered to be entangled in the bulk actin network, which effectively acts as a base for the protruding filaments. However, filaments embedded in semidilute actin solutions have been found to exhibit substantial bending fluctuations in the past [45, 46] and therefore we effectively account for a finite uncertainty in filament orientation by incorporating a distribution of relative branching angles between mother and daughter filaments in the model as is discussed below. Each uncapped filament is growing deterministically at its barbed end with a fixed velocity v_{fil}. Thus we implicitly assume a constant density of actin monomers at the leading edge. Polymerization is quantized such that filaments extent by one building block of length δ_{fil} per unit time. Apart from branching, individual filaments do not interact and hence the local filament density does not alter polymerization. Filament barbed ends within the branching region close to the leading edge are possible candidates for stochastic branching and capping events. While capping is assumed to be a first order reaction in the number of actin barbed ends in the reaction zone, for branching we assume zeroth order. This is motivated by the expectation that the supply of activated Arp2/3 is strongly limited by the availability of NPFs at the leading edge and thus an effective zeroth order branching rate emerges for sufficiently high filament density or low capping rate [47, 48]. In the opposite limit of low filament density, the branching reaction is expected to become first order in the number of filaments; this effectively yields an autocatalytic description [30] that is stationary only at one unique network growth velocity. Therefore in this limit, transitions in the filament orientation distribution are not accessible. However, it has been shown that both, first and zeroth order branching models, can be incorporated within a unified theoretical framework and that the crossover from one regime to the other does not have a direct impact on filament orientation in steady state [48]. As actin networks in most experimental

setups are growing against a finite load of the obstacle and non-constant force–velocity curves are observed, the zeroth order branching regime is expected to dominate the branching kinetics eventually.

The orientation of new filament branches is chosen from a normalized linear combination of two Gaussian probability distributions for the angle between mother and daughter filament with means at $\pm 70°$ and standard deviation $5°$. Red filaments in the illustration are actively growing, while blue filaments indicate capped barbed ends that neither branch nor polymerize anymore and will eventually be outgrown by the bulk network and leave the simulation box at the bottom. In figure 1(b) the top boundary of the yellow branching region defines a rigid obstacle, which excludes volume and thus prevents polymerization above its boundary. As a consequence the fastest filaments which are growing in close to vertical direction are stalled by the obstacle. The vertical velocity of the obstacle is a parameter of the model and set to a constant value v_{nw} directly. This growth velocity should be regarded as the effective outcome in steady state, determined by the details of filament–obstacle interactions (including regulation by biochemical factors). Steady state growth is possible within the velocity range, $0 < v_{nw} < v_{fil}$. Under these conditions a well defined filament number and orientation distribution evolves.

As a powerful analytical alternative to the stochastic framework introduced above, we also develop a deterministic rate equation for dendritic network growth based on earlier approaches of this kind [30–32]. The evolution of the orientation distribution $N(\theta, t)$ of uncapped filament barbed ends integrated over the whole branching region evolves in time by branching and capping events and by filaments growing out of the branching region. This translates into the following ordinary differential equation (ODE):

$$\frac{\partial N(\theta, t)}{\partial t} = \underbrace{\hat{k}_b \int \mathcal{W}(\theta, \theta') N(\theta', t)\, d\theta'}_{\text{branching}} - \underbrace{k_c N(\theta, t)}_{\text{capping}} - \underbrace{k_{gr}(\theta, v_{nw}) N(\theta, t)}_{\text{outgrowth}}. \quad (1)$$

Here again, capping is assumed to be a first order reaction proportional to the number of existing filaments with the proportionality constant, a reaction rate k_c. The probability of branching at a given angle is determined by the weighting factor distribution, $\mathcal{W}(\theta, \theta')$, which is modeled as a linear combination of Gaussians with maxima at branching angles $\pm 70°$ between filaments and standard deviation $\sigma = 5°$. θ is the filament orientation angle measured relative to the vertical direction. The branching reaction is independent of the absolute number of existing filament barbed ends in this model (i.e. a zeroth order reaction). Hence, the branching rate $\hat{k}_b$ is normalized by the total number of new filament ends,

$$\hat{k}_b = \frac{k_b}{\mathcal{W}_{tot}}, \quad \mathcal{W}_{tot} = \int \int \mathcal{W}(\theta, \theta') N(\theta', t)\, d\theta'\, d\theta. \quad (2)$$

The reaction rate k_b indicates the number of new branches per unit time. Most importantly for the specific scope of this work, obstacle velocity and shape enter equation (1) via the outgrowth rate k_{gr}. As filaments are polymerizing with a constant velocity v_{fil} in their individual direction, some filaments will not be able to keep up with the moving obstacle and thus leave the branching region. The precise expression for the rate of outgrowth k_{gr} strongly depends on obstacle geometry and alters the resulting steady state orientation distributions as will be analyzed in detail in the following.

3. Linear obstacle shape

We begin our analysis with linear obstacle shapes as illustrated in figures 1(a) and (b). The obstacle (and therefore the leading edge of the network) moves with a constant velocity v_{nw} toward the top. Our region of interest, the branching region, extends vertically to a distance $d_{\mathrm{br}}^{\perp}$ from the leading edge of the network. The lateral obstacle width is indicated by $d_{\mathrm{br}}^{=}$.

3.1. Flat large obstacle

For obstacles that are laterally widely extended, for instance the leading edge at the front of the lamellipodium in a migrating cell, we have $d_{\mathrm{br}}^{=} \gg d_{\mathrm{br}}^{\perp}$ and thus horizontal filament outgrowth can be neglected locally. Mathematically, this means that we can use periodic boundary conditions in the horizontal direction. This case has been analyzed before in a similar manner as done below for finite-sized and curved obstacles [32], and therefore we recapitulate the most important results as a reference case. In this simple case, outgrowth of filaments from the branching region can only occur in negative normal direction. While the network grows with velocity v_{nw} in positive normal direction, single filaments grow with velocity v_{fil} in their individual direction. The projected polymerization velocity depends on the filament orientation, as

$$v_{\mathrm{fil}}^{\perp}(\theta) = v_{\mathrm{fil}} \cos \theta. \tag{3}$$

Filaments having a larger absolute orientation than the critical angle

$$\theta_{\mathrm{c}} = \arccos \left(\frac{v_{\mathrm{nw}}}{v_{\mathrm{fil}}} \right) \tag{4}$$

are thus not able to keep up with the speed of the obstacle and are subject to outgrowth with a rate

$$k_{\mathrm{gr}}^{\perp}(\theta, v_{\mathrm{nw}}) = \begin{cases} 0 & \text{if} |\theta| \leqslant \theta_{\mathrm{c}}, \\ \frac{v_{\mathrm{nw}} - v_{\mathrm{fil}} \cos \theta}{(d_{\mathrm{br}}^{\perp}/2)} & \text{if } |\theta| > \theta_{\mathrm{c}}. \end{cases} \tag{5}$$

The factor 2 results from the assumption that new filaments branch-off from existing filaments on average in the center of the branching region of vertical width $d_{\mathrm{br}}^{\perp}$. Outgrowth vanishes for filaments with an orientation smaller than a critical angle θ_{c} and from there increases to its maximum at $|\theta| = 180°$.

     We solve equation (1) numerically by introducing $360°$ angle bins and iterating the equations until a steady state is achieved, which then can be compared to the results of the stochastic computer simulations. In order to achieve a deeper understanding, we also introduced a coarse-grained version of equation (1) that can be treated analytically. In equation (1), the number of filament ends in the branching region with angles between θ and $\theta + \mathrm{d}\theta$ is given by $N(\theta, t)\,\mathrm{d}\theta$. By extending this integration to sufficiently large ($\Delta\theta = 35°$) angle bins

$$N_{\bar{\theta}} = \int_{\bar{\theta} - \Delta\theta/2}^{\bar{\theta} + \Delta\theta/2} N(\theta', t)\,\mathrm{d}\theta', \tag{6}$$

and further assuming that branching is restricted to pairs of angle bins with a relative angle difference of $70°$, a system of five coupled ODEs results:

$$\frac{\partial N_{-70°}}{\partial t} = \frac{1}{2}\hat{k}_{\mathrm{b}} N_{0°} - \left(k_{\mathrm{c}} + k_{\mathrm{gr}}^{\perp}(70°) \right) N_{-70°}, \tag{7}$$

$$\frac{\partial N_{-35°}}{\partial t} = \frac{1}{2}\hat{k}_{\mathrm{b}}N_{+35°} - \left(k_{\mathrm{c}} + k_{\mathrm{gr}}^{\perp}(35°)\right) N_{-35°}, \tag{8}$$

$$\frac{\partial N_{0°}}{\partial t} = \frac{1}{2}\hat{k}_{\mathrm{b}}\left(N_{-70°} + N_{+70°}\right) - k_{\mathrm{c}}N_{0°}, \tag{9}$$

$$\frac{\partial N_{+35°}}{\partial t} = \frac{1}{2}\hat{k}_{\mathrm{b}}N_{-35°} - \left(k_{\mathrm{c}} + k_{\mathrm{gr}}^{\perp}(35°)\right) N_{+35°}, \tag{10}$$

$$\frac{\partial N_{+70°}}{\partial t} = \frac{1}{2}\hat{k}_{\mathrm{b}}N_{0°} - \left(k_{\mathrm{c}} + k_{\mathrm{gr}}^{\perp}(70°)\right) N_{+70°}, \tag{11}$$

with

$$\hat{k}_{\mathrm{b}} = \frac{k_{\mathrm{b}}}{\mathcal{W}_{\mathrm{tot}}} = \frac{k_{\mathrm{b}}}{N_{-70°} + N_{-35°} + N_{0°} + N_{+35°} + N_{+70°}}.$$

Here we have also assumed that branching of filaments with orientations $|\theta| > 87.5°$ can be neglected. The five equations are symmetric around $0°$, and thus only three of them are independent. Nonlinearity and the coupling of all five equations is introduced by the branching term due to the zeroth order branching reaction.

By algebraically solving equations (7)–(11) for the stationary state, we obtain two physically meaningful solutions. The first solution,

$$
\begin{aligned}
N_{-70°}^{\mathrm{ss35}} &= 0, \\
N_{-35°}^{\mathrm{ss35}} &= k_{\mathrm{b}}\frac{1}{4(k_{\mathrm{c}} + k_{\mathrm{gr}}^{\perp}(35°))}, \\
N_{0°}^{\mathrm{ss35}} &= 0, \\
N_{+35°}^{\mathrm{ss35}} &= k_{\mathrm{b}}\frac{1}{4(k_{\mathrm{c}} + k_{\mathrm{gr}}^{\perp}(35°))}, \\
N_{+70°}^{\mathrm{ss35}} &= 0,
\end{aligned}
\tag{12}
$$

represents a dominant $\pm35°$ orientation distribution in the steady state while the second solution,

$$
\begin{aligned}
N_{-70°}^{\mathrm{ss70}} &= k_{\mathrm{b}}\frac{k_{\mathrm{c}} + k_{\mathrm{gr}}^{\perp}(70°) - \sqrt{2k_{\mathrm{c}}\left(k_{\mathrm{c}} + k_{\mathrm{gr}}^{\perp}(70°)\right)}}{2\left(k_{\mathrm{gr}}^{\perp 2}(70°) - k_{\mathrm{c}}^2\right)}, \\
N_{-35°}^{\mathrm{ss70}} &= 0, \\
N_{0°}^{\mathrm{ss70}} &= k_{\mathrm{b}}\frac{1 - \sqrt{\frac{k_{\mathrm{c}} + k_{\mathrm{gr}}^{\perp}(70°)}{2k_{\mathrm{c}}}}}{k_{\mathrm{c}} - k_{\mathrm{gr}}^{\perp}(70°)}, \\
N_{+35°}^{\mathrm{ss70}} &= 0, \\
N_{+70°}^{\mathrm{ss70}} &= k_{\mathrm{b}}\frac{k_{\mathrm{c}} + k_{\mathrm{gr}}^{\perp}(70°) - \sqrt{2k_{\mathrm{c}}\left(k_{\mathrm{c}} + k_{\mathrm{gr}}^{\perp}(70°)\right)}}{2\left(k_{\mathrm{gr}}^{\perp 2}(70°) - k_{\mathrm{c}}^2\right)},
\end{aligned}
\tag{13}
$$

corresponds to a competing $+70/0/-70$ pattern.

The stability of these two fixed points can be analyzed with respect to the parameters k_b, k_c, $k_{gr}^\perp(35°)$, $k_{gr}^\perp(70°)$ and $d_{br}^\perp$ using linear stability analysis. The result of this analysis is independent of the branching rate k_b and therefore this parameter has no influence on the stability of the system. According to equations (12) and (13), however, the total number of filaments in steady state is proportional to k_b and therefore this parameter can be used to adjust the model to experimentally measured densities. The two parameters $k_{gr}^\perp(35°)$ and $k_{gr}^\perp(70°)$ are not independent, but rather both of them are determined by the obstacle velocity v_{nw} as given in equation (5). In the following, we will omit the ill-defined cases $k_c = k_{gr}^\perp(35°) = 0$ and $k_c = k_{gr}^\perp(70°) = 0$, for which the filament number diverges. We find that the stability of both fixed points changes when

$$k_c k_{gr}^\perp(70°) = k_c^2 + 4k_c k_{gr}^\perp(35°) + 2k_{gr}^{\perp 2}(35°) \tag{14}$$

and that either one is asymptotically stable, while the other is a saddle. Thus the simple model suggests that exactly two possible network architectures exist with mutually exclusive stability.

Equation (14) can now be used to obtain the respective network velocity v_{nw} of the transition. For a critical angle $\theta_c \geqslant 70°$ (i.e. $k_{gr}^\perp(70°) = k_{gr}^\perp(35°) = 0$), equation (14) is never satisfied (note that $k_c > 0$). For $35° \leqslant \theta_c < 70°$ (i.e. $k_{gr}^\perp(70°) > 0 \land k_{gr}^\perp(35°) = 0$),

$$v_{nw} = \frac{1}{2} k_c d_{br}^\perp + v_{fil} \cos(70°), \quad \text{for } 35° \leqslant \theta_c < 70° \tag{15}$$

satisfies equation (14). For network velocities with a critical angle $\theta_c < 35°$ (i.e. $k_{gr}^\perp(70°) > k_{gr}^\perp(35°) > 0$), two solutions emerge,

$$v_{nw\,1,2} = \frac{1}{8} \left(-3k_c d_{br}^\perp + 8v_{fil} \cos(35°) \right)$$
$$\pm \frac{1}{8} \sqrt{k_c d_{br}^\perp \left(k_c d_{br}^\perp + 16v_{fil} \cos(35°) - 16v_{fil} \cos(70°) \right)}, \tag{16}$$
$$\text{for } \theta_c < 35°.$$

It turns out that solution equation (15) is valid for network bulk velocities $v_{fil} \cos(35°) \geqslant v_{nw} > v_{fil} \cos(70°)$, while for solution equation (16) to be valid $v_{nw} > v_{fil} \cos(35°)$ has to be satisfied. This is never the case for the negative square-root in equation (16) and so we can neglect this solution in the following. In order to further simplify our equations, we define the reference velocity $u_c \equiv k_c d_{br}^\perp$ resulting from the capping rate. Equations (15) and (16) then become
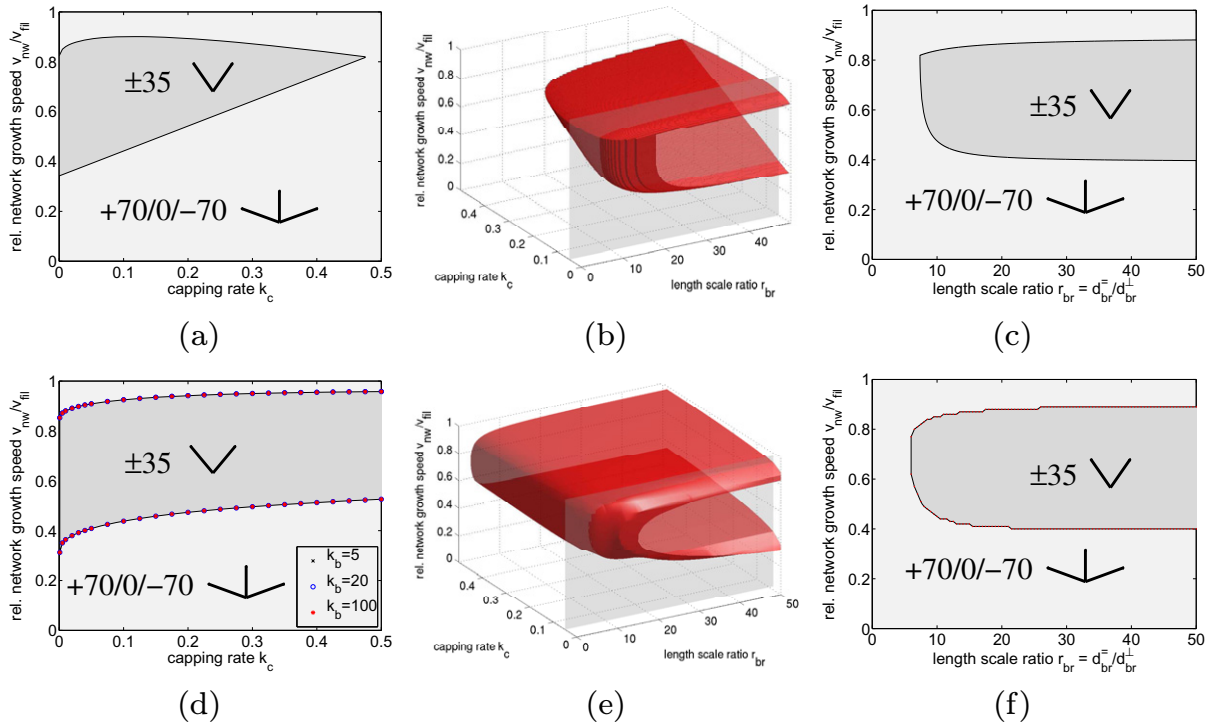
$$\frac{v_{nw}}{v_{fil}} = \frac{1}{2} \frac{u_c}{v_{fil}} + \cos(70°) \tag{17}$$

and

$$\frac{v_{nw}}{v_{fil}} = \frac{1}{8} \left(-3\frac{u_c}{v_{fil}} + 8\cos(35°) \right)$$
$$+ \frac{1}{8} \sqrt{\frac{u_c}{v_{fil}} \left(\frac{u_c}{v_{fil}} + 16\cos(35°) - 16\cos(70°) \right)}, \tag{18}$$

respectively. Thus the capping rate emerges as an essential parameter through the effective velocity u_c.

In figure 2(a) the stability diagram from the analytical analysis is illustrated, showing the regions in which either the $\pm35°$ distribution is asymptotically stable and the $+70/0/-70$

Figure 2. Phase diagram for flat finite-sized obstacles. (a)–(c) Analytical results from linear stability analysis of the simplified continuum model with five angle bins. (d)–(f) Full numerical solution of the rate equation model with 360 angle bins. In (a) and (d), two dimensional slices through the three dimensional hypersurface are plotted within the k_c–v_{nw} plane in the limit of $r_{br} \to \infty$, which corresponds to periodic boundary conditions or very large objects. Panels (b) and (e) show the hyperplane of transition points between the two filament patterns in the full 3D parameter space. In (c) and (f), slice plots in the r_{br}–v_{nw} plane are shown along the transparent gray plane in (b) and (e) at $k_c = 0.05$.

pattern is a saddle or vice versa. In order to compare these results to the full numerical solution of equation (1), we define the relative difference of filaments in the angle bin around $0°$ to the one around $35°$ as an appropriate order parameter in steady state,

$$\mathcal{O} = \frac{N_{0°} - N_{35°}}{N_{0°} + N_{35°}} = [-1, +1]. \tag{19}$$

For a perfect $+70/0/-70$ distribution this parameter will approach $+1$, while for the competing ± 35 pattern it will approach -1. The transition between the two patterns is defined when the order parameter changes its sign. According to this definition of the transition point, it is now possible to numerically solve the continuum model equation (1) and to classify each observed stationary state as one of the two phases. These results are presented as a phase diagram in figure 2(d) and were obtained for different branching rates k_b, which indeed has no significant influence as expected from the analytical considerations. In the solution of the full continuum model the capping rate only has a very limited influence on the stripe-like pattern of the phase diagram. Contrarily, in the phase diagram resulting from linear stability analysis (figure 2(a)),

the ± 35 pattern vanishes at large capping rate. This artifact of the reduced rate equation model is introduced by the assumption that filaments with an orientation larger than $87.5°$ do not branch. As the full rate equation does not share this assumption, it does not predict the elimination of the ± 35 pattern for large capping rate.

3.2. Flat finite-sized obstacle

For flat, but finite-sized obstacle shape, filaments might also leave the branching region horizontally. Therefore a second outgrowth rate needs to be incorporated into the rate equation (equation (1)):

$$k_{gr}^=(\theta, v_{nw}) = \begin{cases} \dfrac{v_{nw} \tan \theta}{(d_{br}^=/2)} & \text{if } |\theta| \leqslant \theta_c, \\[2mm] \dfrac{v_{fil} \sin \theta}{(d_{br}^=/2)} & \text{if } |\theta| > \theta_c. \end{cases} \tag{20}$$

We find that for this scenario, it is still possible to analyze the stability of the fixed points of equations (7)–(11). The only difference that accounts for the change in obstacle geometry at this point is that a combination of outgrowth rates $k_{gr}(\theta) = k_{gr}^\perp(\theta) + |k_{gr}^=(\theta)|$ replaces the term for exclusively orthogonal outgrowth $k_{gr}^\perp(\theta)$ considered in the previous section. For filaments growing in the $N_{0°}$ angle bin, both outgrowth rates vanish, because these filaments are growing at a high enough velocity parallel to the lateral boundaries of the obstacle.

The same arguments as used before also apply for the stability analysis of the steady states here. Hence, we can begin with equation (14) and evaluate the stability of the two steady states according to the adjusted outgrowth rate. To determine the transitions, we will follow a similar strategy as before. Starting from small network velocities v_{nw}, we will treat the different possibilities for the outgrowth rates given in equations (5) and (20) in a case-by-case analysis.

For $\theta_c \geqslant 70°$, the orthogonal outgrowth rates vanish, as all relevant filament orientations grow faster toward the top than the obstacle and are slowed down to v_{nw} in this direction. The outgrowth rates for the different orientation bins therefore read

$$k_{gr}^\perp(\theta) = 0 \text{ and } k_{gr}^=(\theta) = \frac{v_{nw} \tan \theta}{(d_{br}^=/2)} \text{ for } \theta = [35°, 70°]. \tag{21}$$

Inserting $k_{gr} = k_{gr}^\perp + k_{gr}^=$ in equation (14) and omitting again the ill-defined cases of $k_b = 0$, $k_c = 0$ and $d_{br}^= = 0$ here (and additionally $d_{br}^\perp = 0$ in the following), it can be shown that equation (14) is never satisfied.

Increasing the network velocity to the point where $35° \leqslant \theta_c < 70°$ leads to outgrowth rates

$$k_{gr}^\perp(35°) = 0 \text{ and } k_{gr}^\perp(70°) = \frac{v_{nw} - v_{fil} \cos(70°)}{(d_{br}^\perp/2)}, \tag{22}$$

in orthogonal direction according to equation (5) and

$$k_{gr}^=(35°) = \frac{v_{nw} \tan(35°)}{(d_{br}^=/2)} \quad \text{and} \quad k_{gr}^=(70°) = \frac{v_{fil} \sin(70°)}{(d_{br}^=/2)}, \tag{23}$$

in the lateral direction according to equation (20). These rates yield a quadratic equation for the network velocities v_{nw} that satisfy equation (14),

$$0 = v_{\text{nw}}^2 \left[8 \tan^2(35°) \frac{1}{u_{\text{c}}^2 r_{\text{br}}^2} \right] + v_{\text{nw}} \left[8 \tan(35°) \frac{1}{u_{\text{c}} r_{\text{br}}} - 2 \frac{1}{u_{\text{c}}} \right]$$
$$+ \left[1 - 2 v_{\text{fil}} \sin(70°) \frac{1}{u_{\text{c}} r_{\text{br}}} + 2 v_{\text{fil}} \cos(70°) \frac{1}{u_{\text{c}}} \right], \tag{24}$$
$$\text{for } 35° \leqslant \theta_{\text{c}} < 70°.$$

Here, the reference velocity, $u_{\text{c}} = k_{\text{c}} d_{\text{br}}^{\perp}$, together with a new parameter for the length scale ratio in lateral and orthogonal direction, $r_{\text{br}} \equiv d_{\text{br}}^{=}/d_{\text{br}}^{\perp}$, are identified to determine stability.

For a critical angle $\theta_{\text{c}} < 35°$, the adjusted outgrowth rates read

$$k_{\text{gr}}^{\perp}(\theta) = \frac{v_{\text{nw}} - v_{\text{fil}} \cos \theta}{(d_{\text{br}}^{\perp}/2)} \quad \text{and} \quad k_{\text{gr}}^{=}(\theta) = \frac{v_{\text{fil}} \sin \theta}{(d_{\text{br}}^{=}/2)} \quad \text{for } \theta = [35°, 70°]. \tag{25}$$

These rates together with equation (14) and the effective parameters u_{c} and r_{br} can be simplified to a second quadratic equation defining the network velocities at the transitions

$$0 = v_{\text{nw}}^2 \left[8 \frac{1}{u_{\text{c}}^2} \right] + v_{\text{nw}} \left[6 \frac{1}{u_{\text{c}}} - 16 v_{\text{fil}} \cos(35°) \frac{1}{u_{\text{c}}^2} + 16 v_{\text{fil}} \sin(35°) \frac{1}{u_{\text{c}}^2 r_{\text{br}}} \right]$$
$$+ \left[1 + 2 v_{\text{fil}} \cos(70°) \frac{1}{u_{\text{c}}} - 2 v_{\text{fil}} \sin(70°) \frac{1}{u_{\text{c}} r_{\text{br}}} - 8 v_{\text{fil}} \cos(35°) \frac{1}{u_{\text{c}}} + 8 v_{\text{fil}} \sin(35°) \frac{1}{u_{\text{c}} r_{\text{br}}} \right.$$
$$\left. + 8 v_{\text{fil}}^2 \cos^2(35°) \frac{1}{u_{\text{c}}^2} - 16 v_{\text{fil}}^2 \cos(35°) \sin(35°) \frac{1}{u_{\text{c}}^2 r_{\text{br}}} + 8 v_{\text{fil}}^2 \sin^2(35°) \frac{1}{u_{\text{c}}^2 r_{\text{br}}^2} \right], \tag{26}$$
$$\text{for } \theta_{\text{c}} < 35°.$$

According to equations (24) and (26), the regions of stability for the two different stationary orientation patterns in parameter space are illustrated in figure 2(b). As the finite obstacle width introduces an additional independent parameter r_{br}, the full parameter space is now three dimensional. Network growth velocities v_{nw} that fulfill equation (24) together with the condition $v_{\text{fil}} \cos(35°) \geqslant v_{\text{nw}} > v_{\text{fil}} \cos(70°)$ or equation (26) at $v_{\text{nw}} > v_{\text{fil}} \cos(35°)$ are identified as transition points between the different orientation distributions in the parameter space spanned by k_{c}, r_{br} and v_{nw}. In the limit of large length scale ratio, $r_{\text{br}} \to \infty$ (i.e. $d_{\text{br}}^{=} \gg d_{\text{br}}^{\perp}$), lateral outgrowth can be neglected and the phase diagram approaches the results for periodic boundary conditions as given in figure 2(a). For relatively small $r_{\text{br}} \lesssim 7$, the lateral outgrowth of intermediate filament orientations at around $\pm 35°$ is sufficiently large to prevent this orientation pattern from being stable in this model, independent of the growth velocity (cf figure 2(c)).

Using the order parameter equation (19), we numerically sampled the parameter space according to equation (1) with adjusted outgrowth. The isosurface $\mathcal{O}(v_{\text{nw}}, k_{\text{c}}, r_{\text{br}}) = 0$ is extracted from the three dimensional data and shown in figure 2(e). In the limit of large length scale ratio, the results coincide well with the case of periodic boundary conditions (cf figure 2(d)). It is also confirmed that for small values of r_{br} the ± 35 pattern is not stable anymore at intermediate velocities (cf figure 2(f)). Thus the overall agreement between the simple analytical model and the full numerical solution of the rate equation approach is surprisingly good.

Figure 3 compares filament orientation distributions obtained in steady state from stochastic network simulations, the full continuum model and the simplified continuum model.
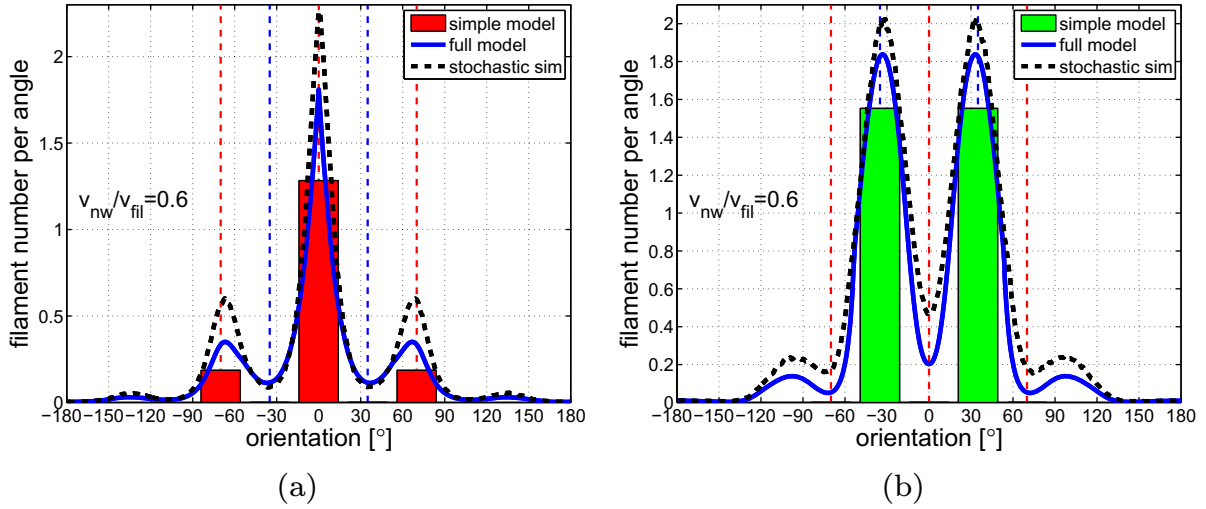
Figure 3. Comparison of the steady state orientation distributions for actin networks growing in the tail of a flat obstacle of finite size at $v_{nw}/v_{fil} = 0.6$, $k_b = 20$, $k_c = 0.05$, $d_{br}^{\perp} = 2\delta_{fil}$ and (a) $r_{br} = 3$, (b) $r_{br} = 20$. The results were obtained according to three different methods, the simplified continuum model (bars), the full continuum model (blue solid line) and stochastic simulations (black dashed line).

The parameters of the two cases shown in (a) and (b) do not differ in their network velocity v_{nw}, but rather only in the obstacle geometry, in this case given by length scale ratio $r_{br} = d_{br}^{=}/d_{br}^{\perp}$. For small $r_{br} = 3$ at intermediate velocities, the ± 35 pattern of the network is not stable anymore and rather the network organizes in the alternative $+70/0/-70$ distribution (cf figure 3(a)). For larger ratio $r_{br} = 20$, the network organizes in the $\pm 35°$ distribution (cf figure 3(b)). In the stochastic simulations, outgrowth rates are not explicitly incorporated, but rather emerge as a direct consequence of the obstacle geometry. Thus the computer simulations nicely validate both, the full and reduced continuum approaches, and all three seem to capture the essential physical mechanisms determining network structure.

3.3. Obstacle with tilted straight contour

It is not trivial to find an explicit expression for the outgrowth rate out of the branching region behind a skewed linear obstacle, which is rotated according to a constant skew angle φ, with $-90° < \varphi < +90°$. However, for reasonably small skew angle φ and width of the orthogonal branching region $d_{br}^{\perp}$ an approximation can be obtained within a rotated coordinate frame, that is adjusted to the constant obstacle skew. Figure 4(a) shows a sketch of the obstacle geometry we are interested in at this point. The branching region is given by a rhomboid, with rotated (or skewed) upper and lower side. The orthogonal width of the branching region $d_{br}^{\perp}$ is again defined parallel to the lateral sides of the obstacle, while its horizontal width is given by $d_{br}^{=}$. Network velocity v_{nw} is defined as before in the vertical direction. To find an explicit expression for the rates of filament outgrowth, a rotation of the coordinate frame to the point where the skew angle φ of the branching region vanishes simplifies the situation (figure 4(b)). In this frame the obstacle appears flat horizontally, very similar to the setup analyzed before in section 3.2.
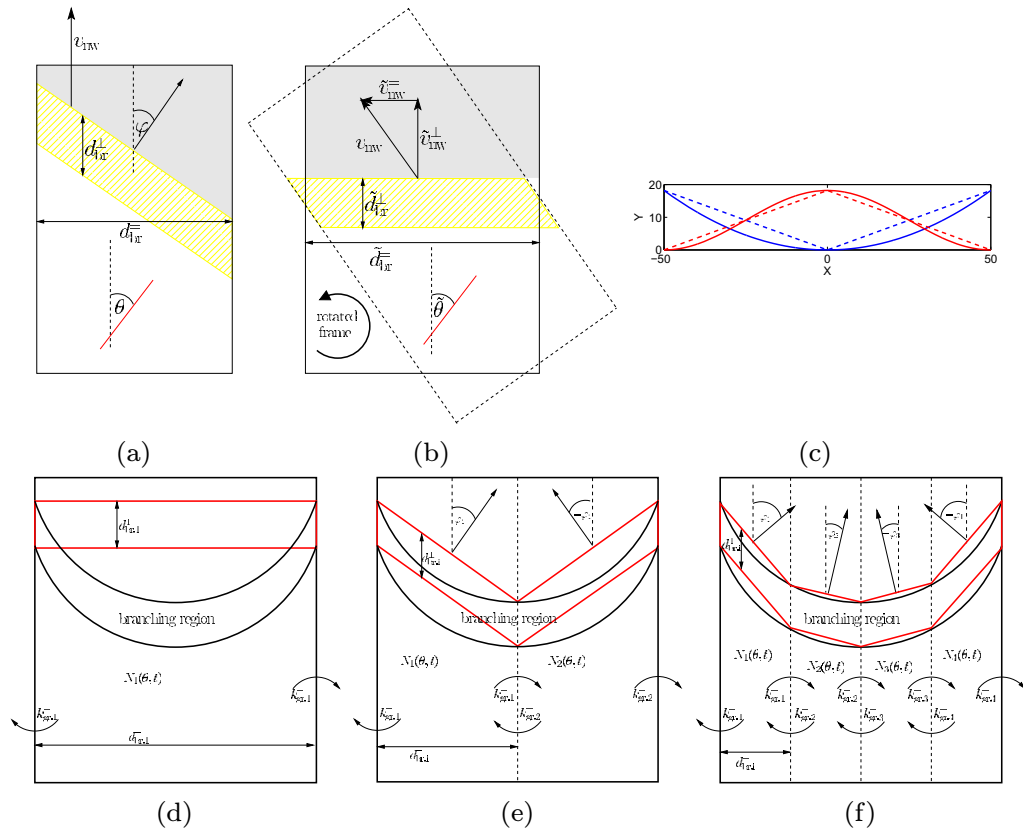
Figure 4. (a), (b) Within a rotated coordinate frame, the continuum model (equation (1)) is applicable to treat filament networks growing behind a skewed linear obstacle. (a) *Lab frame*: a generic skewed linear obstacle with skew angle φ. (b) *Obstacle frame*: the coordinate system is rotated by its skew angle φ counter-clockwise. In this frame the initial skew of the system is expressed by an additional finite lateral motion at velocity $\tilde{v}_{nw}^{=}$ of an otherwise flat obstacle moving at $\tilde{v}_{nw}^{\perp}$. (c) Parabolic (blue) and cosine (red) nonlinear obstacle shapes. The solid lines indicate the nonlinear obstacle shape, while the dashed line corresponds to a piecewise-linear triangular approximation. Horizontally the parabolic shape has a finite width, while the cosine obstacle shape is analyzed in periodic conditions laterally. (d)–(f) Piecewise-linear approximations of a parabola-like obstacle geometry. (d) The simplest approximation is a flat linear obstacle. (e) Due to the left–right symmetry in obstacle shape, in higher order approximations of the nonlinear obstacle (e.g. the triangular approximation shown here), only half of the number of sections have to be considered explicitly. The boundary condition at the center of the box has to be adjusted accordingly. (f) Subdividing the piecewise-linear sections again and again leads to ever higher accuracy in the approximation of the nonlinear obstacle shape and to ever smaller horizontal width of each subsection, $d_{br,i}^{=} = d_{br}^{=}/n$. Approaching the continuum limit, $n \to \infty$, yields a PDE-model for nonlinear obstacle shapes.

The finite skew angle φ, however, manifests in a non-vanishing lateral network growth velocity $\tilde{v}_{nw}^{=}$, while the vertical propulsion speed of the obstacle is the orthogonal part of the network velocity in this frame, $\tilde{v}_{nw}^{\perp}$. (Where applicable, we will denote variables defined in the rotated

coordinate frame by ˜ .) In the following we will refer to the original coordinate system figure 4(a) as the *lab frame* and to the rotated picture figure 4(b) as the *obstacle frame*.

Using the transformation to the obstacle frame for a given skew angle φ, we can now deduce the relevant parameters. The filament orientation angles $\tilde{\theta}$ are given relative to the obstacle, i.e. for $\tilde{\theta} = 0°$ filaments are growing vertically in the rotated frame. The two components of obstacle growth velocity are given by

$$\tilde{v}_{nw}^{\perp}(\varphi) = v_{nw} \cos\varphi \quad \text{and} \quad \tilde{v}_{nw}^{=}(\varphi) = v_{nw} \sin\varphi. \tag{27}$$

The two obstacle diameters, which scale the vertical and horizontal outgrowth rates are,

$$\tilde{d}_{br}^{\perp}(\varphi) = d_{br}^{\perp} \cos\varphi \quad \text{and} \quad \tilde{d}_{br}^{=}(\varphi) = \frac{d_{br}^{=}}{\cos\varphi}. \tag{28}$$

According to these definitions, we can now reformulate the continuum description in the obstacle frame. The rate equation (1) for the temporal evolution of orientation dependent filament density remains unchanged with respect to the transformed orientation angles $\tilde{\theta}$, however with adjusted outgrowth rate $k_{gr}(\theta, v_{nw})$ given by the sum of orthogonal outgrowth,

$$\tilde{k}_{gr}^{\perp}(\tilde{\theta}, \varphi, v_{nw}) = \begin{cases} 0 & \text{if } |\tilde{\theta}| \leqslant \tilde{\theta}_c, \\ \dfrac{\tilde{v}_{nw}^{\perp}(\varphi) - v_{fil} \cos\tilde{\theta}}{(\tilde{d}_{br}^{\perp}(\varphi)/2)} & \text{if } |\tilde{\theta}| > \tilde{\theta}_c \end{cases} \tag{29}$$

and the absolute value of lateral outgrowth,

$$\tilde{k}_{gr}^{=}(\tilde{\theta}, \varphi, v_{nw}) = \begin{cases} \dfrac{\tilde{v}_{nw}^{=}(\varphi) + \tilde{v}_{nw}^{\perp}(\varphi) \tan\tilde{\theta}}{(\tilde{d}_{br}^{=}(\varphi)/2)} & \text{if } |\tilde{\theta}| \leqslant \tilde{\theta}_c, \\ \dfrac{\tilde{v}_{nw}^{=}(\varphi) + v_{fil} \sin\tilde{\theta}}{(\tilde{d}_{br}^{=}(\varphi)/2)} & \text{if } |\tilde{\theta}| > \tilde{\theta}_c \end{cases} \tag{30}$$

with,

$$\tilde{\theta}_c = \arccos\left(\frac{\tilde{v}_{nw}^{\perp}(\varphi)}{v_{fil}}\right). \tag{31}$$

The lateral outgrowth rate compared to equation (20) is biased by the finite horizontal velocity of the network in the obstacle frame $\tilde{v}_{nw}^{=}$. This additional feature also breaks the symmetry in the resulting steady state filament orientation distributions. The sign of the outgrowth rate determines, whether filaments are growing out to the left ($\tilde{k}_{gr}^{=} < 0$) or the right ($\tilde{k}_{gr}^{=} > 0$) of the branching region, which is only relevant when keeping track of the filaments' fate after outgrowth. This will become important later in section 4.1, but at this point the sign of lateral outgrowth is suppressed.

To test our approximation, we again compared steady state filament orientation distributions, obtained by numerical iteration of equation (1) within the obstacle frame and subsequent transformation to the lab frame, against stochastic simulations. Typical cases are shown in figures 5(a)–(d) for a moderate obstacle skew angle of $\varphi = 20°$, fast and slow network velocity in the lab frame v_{nw}, and small and large horizontal obstacle diameter as indicated by the length scale ratio r_{br} (figure 5 also shows results obtained with a PDE-model which we will introduce below). If the results are interpreted directly in the adjusted obstacle frame,
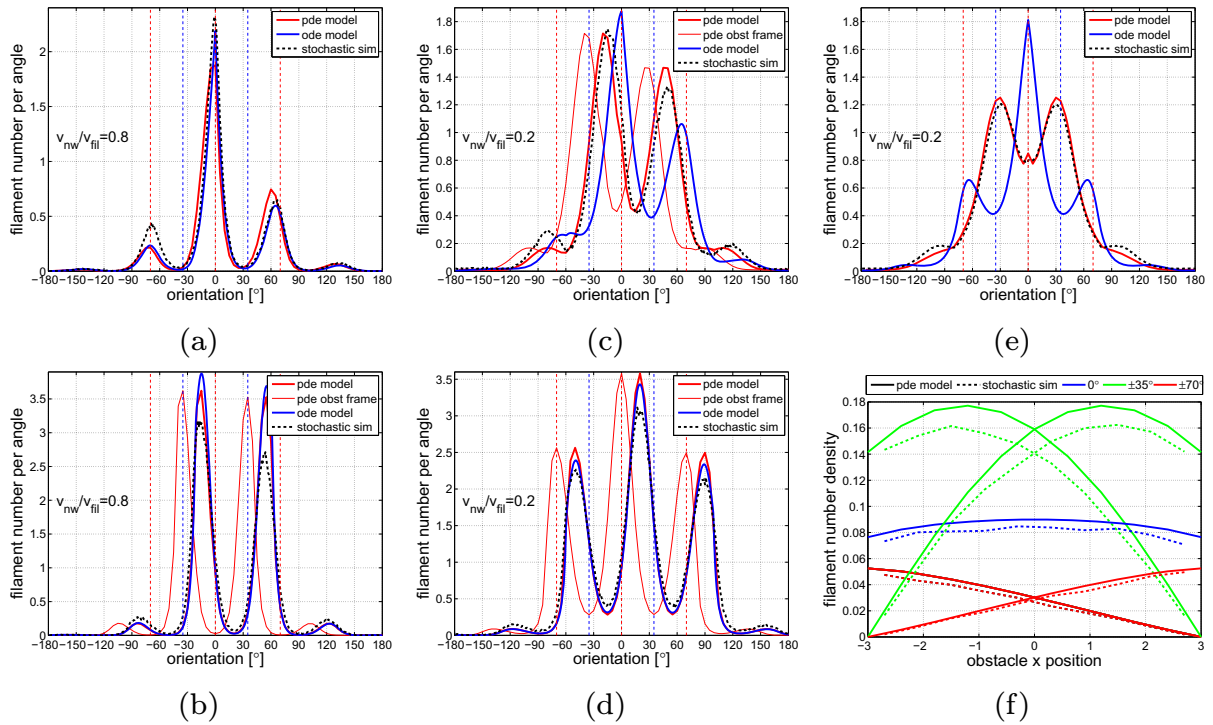
Figure 5. (a)–(d) Representative results for the stationary filament orientation distributions of a linear tilted obstacle obtained in the PDE-model (thick red solid line), the ODE-model (equation (1)) (blue solid line) and in stochastic network simulations (black dashed line). Where applicable also the transformation of the resulting PDE-model distributions to the obstacle frame is shown (thin red line). Here the orientation patterns can be interpreted as ± 35 and $+70/0/-70$ patterns, that were also active in the tail of flat linear obstacles (cf figures 2 and 3). The active parameters are, $\varphi = 20°$, $k_b = 20$, $d_{br}^{\perp} = 2\delta_{fil}$ and (a) $r_{br} = 3$, $v_{nw}/v_{fil} = 0.8$. (b) $r_{br} = 100$, $v_{nw}/v_{fil} = 0.8$. (c) $r_{br} = 3$, $v_{nw}/v_{fil} = 0.2$. (d) $r_{br} = 100$, $v_{nw}/v_{fil} = 0.2$. (e) and (f) Comparison of the steady state solution for a non-periodic linear flat obstacle from the ODE-model (equation (1)), the PDE-model (equation (32)) and stochastic network simulations. (e) For small $r_{br} = 3$, the ODE-solution (blue line) predicts the absence of a ± 35 orientation distribution (cf figure 2). However, for relatively low network velocity at $v_{nw}/v_{fil} = 0.2$, the spatially resolved PDE-solution (red line) as well as network simulations (black dashed line) yield such a pattern. (f) The spatial filament distributions are far from uniform. Results from PDE-model (solid) and stochastic network simulation (dashed) rather show an accumulation of filaments at the lateral flanks of the obstacle, and therefore also horizontal outgrowth rates and as a direct consequence, the resulting orientation distribution averaged over the whole branching region differs from the prediction of the ODE-model.

very similar orientation patterns as the familiar ± 35 and $+70/0/-70$ peaked distributions are realized in steady state. In the limit of very large length scale ratio r_{br}, outgrowth in the lateral direction can be neglected again and the resulting patterns resemble orientation patterns for

a network growing behind a large obstacle, only now within the rotated obstacle frame (cf figures 5(b) and (d)). For small r_{br} in combination with a relatively high obstacle velocity, horizontal outgrowth cannot be neglected and the orientation distribution has to be interpreted in the lab frame (figure 5(a)). In between a transition occurs where the solutions from stochastic simulations already have to be interpreted in the obstacle frame, while results from the rate equation model are still to be interpreted directly in the lab frame (figure 5(c)). The reason for this is the spatial resolution in the lateral filament position, which is introduced in filament based stochastic simulations and neglected in the continuum model. Laterally non-uniform spatial filament distributions lead to differences in the effective outgrowth of filaments to the sides of the branching region. In order to include a similar spatial resolution in the continuum model, in the following we will incorporate an additional advection term in the equation. In this way it will also become possible to treat nonlinear obstacle shapes within the continuum description.

4. Nonlinear obstacle shape

In this section, we focus on actin network dynamics in the tail of curved (i.e. nonlinear) obstacle geometries. The definitions of the relevant parameters stay the same in this geometry as introduced in figure 1(a). Figure 1(c) features a representative steady state network from stochastic simulation. In the following, we will stepwise extend the continuum model equation (1) with the goal to also incorporate nonlinear obstacle shapes in the description. We will do this first within an adjusted ODE model in a piecewise-linear approximation of the obstacle surface and then within a PDE model, where an advection term will explicitly govern lateral filament growth in the rate equation, additional to the reaction terms.

4.1. Piecewise-linear obstacle approximation

Nonlinear obstacle shapes can be treated within a piecewise-linear approximation for the obstacle surface in which the ODE-model from above is still applicable. The construction of this approximation is sketched in figures 4(d)–(f) for a parabola-like curved obstacle surface. The branching region is divided laterally in n sections of equal size $d_{br,i}^{=} = d_{br}^{=}/n$ $(i = 1, \ldots, n)$. The orthogonal width of the branching region in each section remains unchanged at $d_{br,i}^{\perp} = d_{br}^{\perp}$. The resulting obstacle approximation is a combination of lateral sections with skewed linear shape according to skew angles φ_i, very similar to the obstacles discussed before. The individual sections (i.e. the ODE-model equation of each section) are coupled to their direct neighbors via the lateral outgrowth rates $k_{gr,i}^{=}$ to the left and right boundaries as indicated in the sketch. In case of periodic lateral boundary conditions of the obstacle, sections $i = 1$ and n are also coupled via outgrowth. Individual outgrowth rates within the local obstacle frame of each section can then be formulated according to equations (29) and (30) as before.

Assuming a single linear obstacle is the simplest approximation of a nonlinear geometry (figure 4(d)). To increase accuracy, the obstacle can be subdivided laterally in ever smaller subsections. Due to the left–right symmetry of many biologically relevant obstacle shapes (e.g. the parabola-like shape in the sketch) it is sufficient to obtain results in one half-space of the obstacle geometry. This translates into a problem of $n/2$ coupled ODEs for an even number of subsections in the piecewise-linear approximation. In order to exploit this symmetry, lateral outgrowth from the section adjacent to the middle of the box has to be adjusted: filaments that would leave the section in the middle toward the other side of the obstacle are reinjected
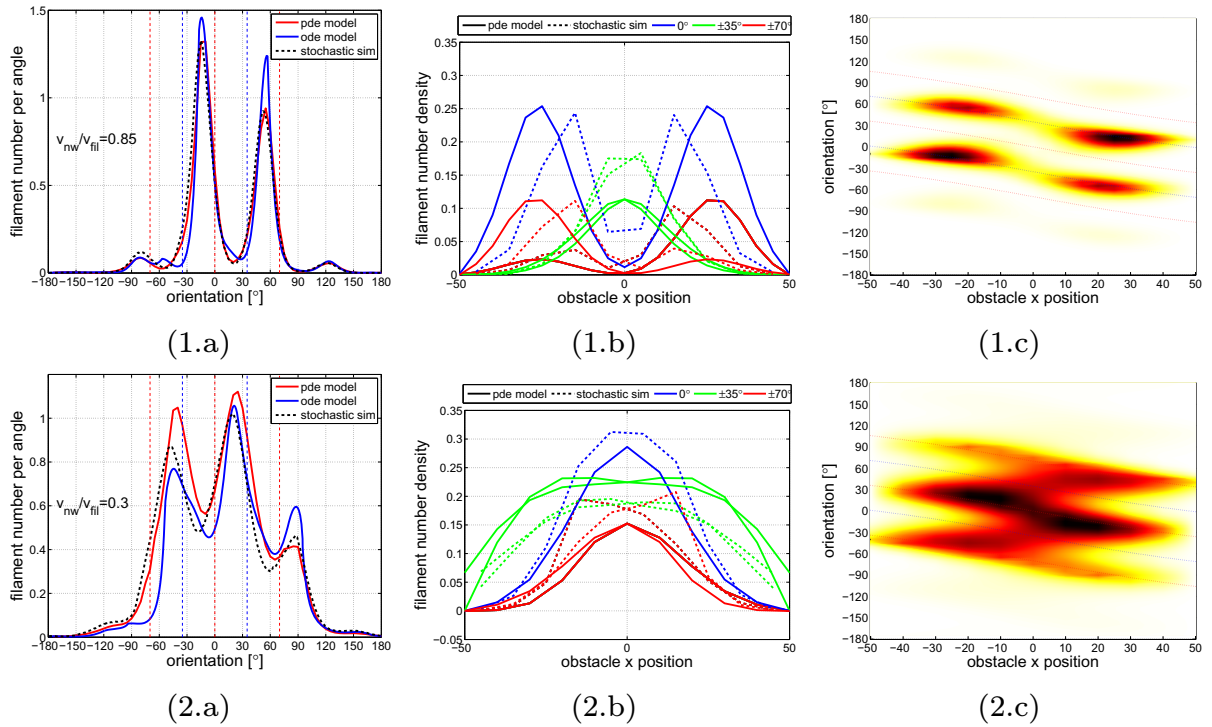
Figure 6. Typical stationary filament distributions in the tail of a non-periodic parabolic obstacle (cf blue solid line in figure 4(c)) for the parameter combinations, $\bar{\varphi} = 20°$, $r_{br} = 50$, $d_{br}^{\perp} = 2\delta_{fil}$, $k_b = 20$, $k_c = 0.05$; (1) $v_{nw}/v_{fil} = 0.85$; (2) $v_{nw}/v_{fil} = 0.3$. (a) Filament orientation distributions spatially averaged laterally over the left hand side half space behind the symmetric obstacle. For comparison the results from PDE-model, ODE-model in triangular approximation (as illustrated by the dashed blue line in figure 4(c)) and stochastic simulations are shown. (b) Spatial distributions of characteristic filament angles at $\theta = 0°$, $\pm 35°$ and $\pm 70°$. Interpretation in the lab frame indicates coexistence of the competing ± 35 and $+70/0/-70$ patterns at different lateral positions along the obstacle. (c) Heat map of the spatially resolved filament orientation distributions, where cooler colors indicate increasing filament density. Plotting dashed lines at characteristic angles at $\tilde{\theta} = 0°$, $\pm 35°$ and $\pm 70°$ in the obstacle frame indicates that in this frame a single familiar pattern dominates. The apparent coexistence of different patterns is artificially introduced due to a misinterpretation of the results in the lab frame.

again at this position with mirrored orientation, $\theta \rightarrow -\theta$. For instance in case of a triangular approximation of the nonlinear obstacle (figure 4(e)), only the outgrowth behavior at one boundary needs adjustment compared to the problem of a skewed linear obstacle shape that was already discussed before. Figures 6(a) and 7(a) show steady state filament orientation distributions for a laterally non-periodic parabola and periodic-cosine shape obtained by the ODE-model in triangular approximation respectively. The nonlinear obstacle shapes together with their respective triangular approximations are illustrated in figure 4(c). To parametrize nonlinear parabola and cosine geometries in this context, we are using the left hand side skew

(1.a) (1.b) (1.c)

(2.a) (2.b) (2.c)
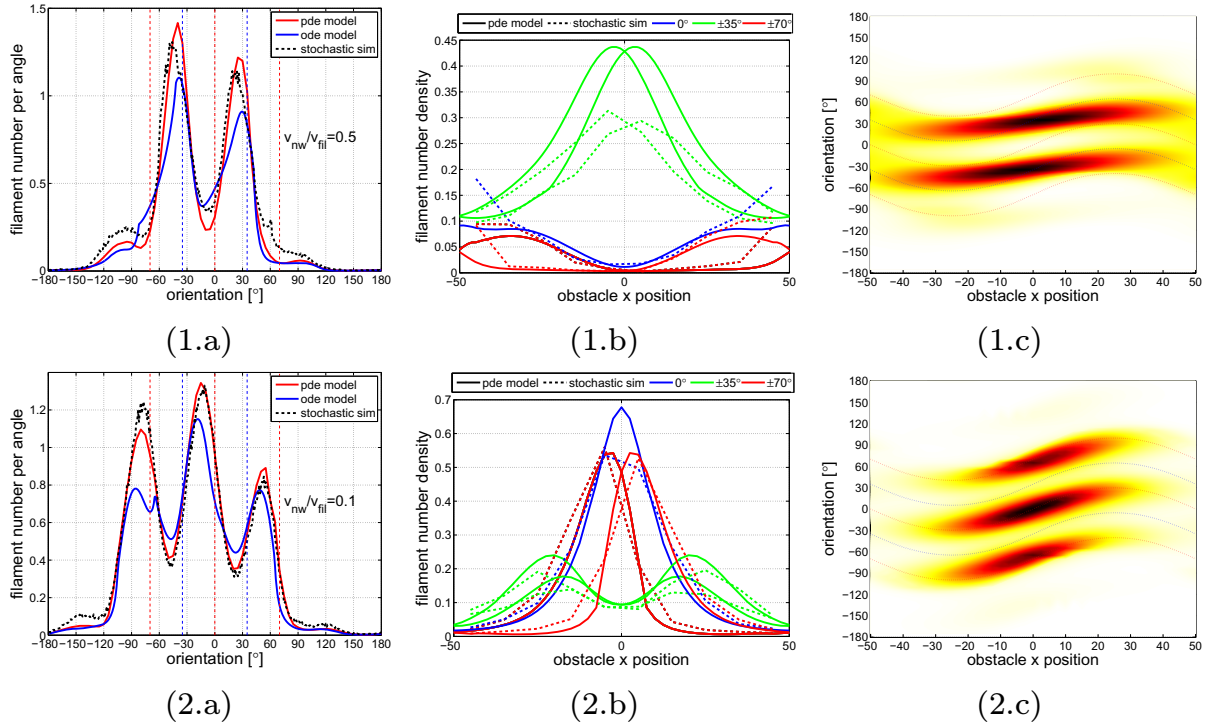
Figure 7. Same as figure 6 for a periodic-cosine shaped obstacle as illustrated by the solid red line in figure 4(c). Active parameters are $\bar{\varphi} = -20°$, $r_{\mathrm{br}} = 50$, $d_{\mathrm{br}}^{\perp} = 2\delta_{\mathrm{fil}}$, $k_{\mathrm{b}} = 20$, $k_{\mathrm{c}} = 0.05$; (1) $v_{\mathrm{nw}}/v_{\mathrm{fil}} = 0.5$; (2) $v_{\mathrm{nw}}/v_{\mathrm{fil}} = 0.1$. Again an apparent coexistence of competing patterns disappears when results are interpreted in the obstacle frame, that is locally orthogonal to the obstacle surface.

angle of the triangular obstacle approximation $\bar{\varphi}$ in combination with the horizontal width of the obstacle indicated by r_{br}.

4.2. Reaction–advection equation

The continuum limit of an infinitely large number of piecewise-linear subsections, each of infinitesimal width, yields a PDE-model for nonlinear obstacle shapes. The model equations in this limit are complemented by an additional filament advection term, similar to hydrodynamic models, that incorporates lateral filament growth in equation (1),

$$\frac{\partial N(\theta, x, t)}{\partial t} + \frac{\partial (N(\theta, x, t) v_{\mathrm{fil}}^{=}(\theta, \varphi, v_{\mathrm{nw}}))}{\partial x} = \hat{k}_{\mathrm{b}} \int \mathcal{W}(\theta, \theta') N(\theta', x, t)\, \mathrm{d}\theta'$$
$$- k_{\mathrm{c}} N(\theta, x, t) - k_{\mathrm{gr}}^{\perp}(\theta, \varphi, v_{\mathrm{nw}}) N(\theta, x, t), \tag{32}$$

with the horizontal filament growth speed, $v_{\mathrm{fil}}^{=}(\theta, \varphi, v_{\mathrm{nw}})$, and the vertical outgrowth rate in the lab frame, $k_{\mathrm{gr}}^{\perp}(\theta, \varphi, v_{\mathrm{nw}})$. Both, filament growth velocity and outgrowth rate are functions of filament orientation θ as well as the local obstacle skew angle $\varphi(x)$, which is active at lateral position x. Here again, we average outgrowth of filaments in the vertical direction by an effective rate, while horizontal growth is now spatially resolved due to the additional advection term.

IOP Institute of Physics ⬥ DEUTSCHE PHYSIKALISCHE GESELLSCHAFT

For arbitrary obstacle shape, that can be expressed in terms of an analytic function $o(x)$, the local skew angle can be written as

$$\varphi(x) = -\arctan\left(\frac{\partial o(x)}{\partial x}\right).\tag{33}$$

The two components of the filament growth velocities within the *local* obstacle frame can thus be written as

$$\tilde{v}_{\mathrm{fil}}^{\perp}(\tilde{\theta}, \varphi, v_{\mathrm{nw}}) = \begin{cases} 0 & \text{if } |\tilde{\theta}| \leqslant \tilde{\theta}_{\mathrm{c}}, \\ \tilde{v}_{\mathrm{nw}}^{\perp}(\varphi) - v_{\mathrm{fil}}\cos\tilde{\theta} & \text{if } |\tilde{\theta}| > \tilde{\theta}_{\mathrm{c}} \end{cases}\tag{34}$$

and

$$\tilde{v}_{\mathrm{fil}}^{=}(\tilde{\theta}, \varphi, v_{\mathrm{nw}}) = \begin{cases} \tilde{v}_{\mathrm{nw}}^{=}(\varphi) + \tilde{v}_{\mathrm{nw}}^{\perp}(\varphi)\tan\tilde{\theta} & \text{if } |\tilde{\theta}| \leqslant \tilde{\theta}_{\mathrm{c}}, \\ \tilde{v}_{\mathrm{nw}}^{=}(\varphi) + v_{\mathrm{fil}}\sin\tilde{\theta} & \text{if } |\tilde{\theta}| > \tilde{\theta}_{\mathrm{c}}, \end{cases}\tag{35}$$

with the components of the obstacle velocity, $\tilde{v}_{\mathrm{nw}}^{\perp}(\varphi)$ and $\tilde{v}_{\mathrm{nw}}^{=}(\varphi)$, defined as in equation (27) and $\tilde{\theta}_{\mathrm{c}}$ as in equation (31). A transformation (i.e. rotation) from the local obstacle frame into the local lab frame at each horizontal position along the obstacle surface subsequently leads to filament growth velocities, which enter the PDE-model equation (32) due to vertical outgrowth and advection,

$$v_{\mathrm{fil}}^{\perp}(\theta, \varphi, v_{\mathrm{nw}}) = \tilde{v}_{\mathrm{fil}}^{\perp}(\tilde{\theta}, \varphi, v_{\mathrm{nw}})\cos\varphi + \tilde{v}_{\mathrm{fil}}^{=}(\tilde{\theta}, \varphi, v_{\mathrm{nw}})\sin\varphi,$$

$$v_{\mathrm{fil}}^{=}(\theta, \varphi, v_{\mathrm{nw}}) = -\tilde{v}_{\mathrm{fil}}^{\perp}(\tilde{\theta}, \varphi, v_{\mathrm{nw}})\sin\varphi + \tilde{v}_{\mathrm{fil}}^{=}(\tilde{\theta}, \varphi, v_{\mathrm{nw}})\cos\varphi.\tag{36}$$

Note, that filaments with a positive $v_{\mathrm{fil}}^{\perp}(\theta, \varphi)$ are growing vertically in opposite direction to the obstacle. Using these expressions, we can now rewrite the advection term in equation (32) as

$$\frac{\partial\left(Nv_{\mathrm{fil}}^{=}\right)}{\partial x} = v_{\mathrm{fil}}^{=}\frac{\partial N}{\partial x} + N\frac{\partial v_{\mathrm{fil}}^{=}}{\partial x} = v_{\mathrm{fil}}^{=}\frac{\partial N}{\partial x} + N\frac{\partial v_{\mathrm{fil}}^{=}}{\partial\varphi}\frac{\partial\varphi}{\partial x},\tag{37}$$

with

$$\frac{\partial v_{\mathrm{fil}}^{=}}{\partial\varphi} = -\frac{\partial\left(\tilde{v}_{\mathrm{fil}}^{\perp}\sin\varphi\right)}{\partial\varphi} + \frac{\partial\left(\tilde{v}_{\mathrm{fil}}^{=}\cos\varphi\right)}{\partial\varphi},\tag{38}$$

and substituting equation (34),

$$\frac{\partial\left(\tilde{v}_{\mathrm{fil}}^{\perp}\sin\varphi\right)}{\partial\varphi} = \begin{cases} 0 & \text{if } |\tilde{\theta}| \leqslant \tilde{\theta}_{\mathrm{c}}, \\ -v_{\mathrm{nw}}\sin^2\varphi + v_{\mathrm{nw}}\cos^2\varphi - v_{\mathrm{fil}}\cos\tilde{\theta}\cos\varphi - v_{\mathrm{fil}}\sin\varphi\sin\tilde{\theta} & \text{if } |\tilde{\theta}| > \tilde{\theta}_{\mathrm{c}} \end{cases}\tag{39}$$

and equation (35),

$$\frac{\partial\left(\tilde{v}_{\mathrm{fil}}^{=}\cos\varphi\right)}{\partial\varphi}$$

$$= \begin{cases} v_{\mathrm{nw}}\cos^2\varphi - v_{\mathrm{nw}}\sin^2\varphi - 2v_{\mathrm{nw}}\cos\varphi\sin\varphi\tan\tilde{\theta} - v_{\mathrm{nw}}\cos^2\varphi\cos^{-2}\tilde{\theta} & \text{if } |\tilde{\theta}| \leqslant \tilde{\theta}_{\mathrm{c}}, \\ v_{\mathrm{nw}}\cos^2\varphi - v_{\mathrm{nw}}\sin^2\varphi - v_{\mathrm{fil}}\sin\tilde{\theta}\sin\varphi - v_{\mathrm{fil}}\cos\varphi\cos\tilde{\theta} & \text{if } |\tilde{\theta}| > \tilde{\theta}_{\mathrm{c}}, \end{cases}\tag{40}$$

and using equation (33),

$$\frac{\partial \varphi}{\partial x} = \frac{-\frac{\partial^2 o(x)}{\partial x^2}}{1 + \left(\frac{\partial o(x)}{\partial x}\right)^2}. \tag{41}$$

As we average outgrowth in the vertical direction by the rate $k_{gr}^{\perp}(\theta, \varphi, v_{nw})$ in the lab frame, while horizontal growth is now spatially resolved, we have to take into account the finite lateral movement of filaments along the obstacle geometry, when considering filaments growing out of the branching region vertically. To approximate the filament outgrowth rate accordingly, we again assume a locally linear obstacle shape at each horizontal position to find an analytical expression for the outgrowth rate in equation (32),

$$k_{gr}^{\perp}(\theta, \varphi, v_{nw}) = \sqrt{\frac{v_{fil}^{\perp 2} + v_{fil}^{= 2}}{\left(\frac{d_{br}^{\perp}/2}{v_{fil}^{\perp}/v_{fil}^{=} - \tan\varphi}\right)^2 + \left(\frac{d_{br}^{\perp}/2}{1 - v_{fil}^{=}/v_{fil}^{\perp} \tan\varphi}\right)^2}}. \tag{42}$$

To calculate steady state filament orientation distributions from this PDE-model, equations (32)–(42) can be numerically iterated in discretized space and time using for instance a second order upwind scheme for the spatial differential in combination with an Euler method for temporal iteration [49]. For this procedure, we are using a uniform filament distribution in space and orientation as initial condition and, dependent on the specific obstacle shape considered, either periodic boundary conditions or zero filament density at the respective inflow boundary.

4.3. Linear obstacle shape revisited

The important advantage of using the PDE-model equation (32) compared to the initial ODE equation (1) to solve for steady state filament patterns clearly lies in its additional spatial resolution. This benefit not only increases the applicability of the model to a broader range of obstacle shapes, but also manifests itself when solving for specific parameter combinations for simple non-periodic linear flat obstacles that have been already accessible using the initial ODE equations. Figure 5(e) illustrates the steady state filament orientation distributions averaged over the whole branching region behind an obstacle of small width (i.e. $r_{br} = 3$). For such laterally small and flat obstacles, the ODE-model predicted the absence of the ± 35 orientation pattern for arbitrary obstacle velocities v_{nw} (cf figure 2). Due to their additional spatial resolution horizontally, the PDE-model as well as results from stochastic network simulations yield this orientation distribution nevertheless for a small range of parameters at relatively slow obstacle velocity, $v_{nw}/v_{fil} = 0.2$. As shown in figure 5(f), the spatial steady state filament distributions from the PDE-model are non-uniform horizontally and in good agreement to results from stochastic simulations. This has an impact on the effective lateral outgrowth of filaments in the model and thus is able to change the final (spatially averaged) filament distributions characteristically as shown in this example.

4.4. Parabolic and periodic-cosine obstacle shapes

The PDE-model allows us to systematically analyze actin networks in the tail of nonlinear obstacle shapes. As a proof of principle, in the following we have chosen two different obstacle shapes which are motivated by highly relevant biological examples. On the one hand, we model

a laterally non-periodic parabolic obstacle shape (blue solid line in figure 4(c)) which is a first approximation for the spherical or ellipsoidal shape of actin-propelled intracellular pathogens. On the other hand, actin growth behind a periodic-cosine geometry (red solid line in figure 4(c)) is analyzed, motivated by the laterally widely spread but corrugated leading edge of a crawling or spreading cell.

In figures 6 and 7, the resulting steady state patterns from the three different modeling approaches (PDE-model, ODE-model in triangular piecewise-linear approximation and stochastic network simulations) are shown for specific parameter combinations. In (a) the filament orientation distributions spatially integrated over the left side of the symmetric obstacle are shown. Here, the PDE-model corresponds very well to stochastic network simulations. Despite the rough piecewise-linear approximation of the nonlinear obstacle shape in the ODE-model, the results capture the overall characteristic of the resulting network pattern very well. Subfigures (b) illustrate the resulting spatial distributions of certain characteristic filament angles. For specific parameter cases separate spatial domains emerge over the horizontal obstacle dimension, in which the signature of the two alternative steady state network patterns, i.e. $+70/0/-70$ and ±35, are observed. For a better overview over the complete spatially resolved orientation patterns from the PDE-model, figures 6(c) and 7(c) illustrate the two dimensional filament distribution in heat plots, where regions of cooler color indicate higher filament density. The apparent coexistence of alternative patterns resolves when additional dotted lines are included in the heat map to indicate local filament orientations that correspond to the characteristic orientations $\tilde{\theta} = 0°$, $\pm35°$, $\pm70°$ within the obstacle frame, locally orthogonal to the obstacle surface along its contour. Although coexistence of alternative filament orientations is present in the lab frame, an interpretation in the local obstacle frame yields one unique pattern only that is present along the lateral extension of the obstacle.

5. Discussion

In this paper, we have introduced several theoretical approaches at different levels of complexity with the common goal to predict actin filament orientation patterns at the surface of stiff two dimensional obstacles, whose surfaces promote growth of actin networks. This problem is not only central for many important health and disease related biological phenomena, such as migration of animal cells or propagation of pathogens in their host, it is also a prominent example for a physical process whose properties emerge on a mesoscopic length scale in relative independence of the details of the underlying molecular processes. For example, the competition of the two fundamentally different network architectures discussed here does not rely on the exact value of the branching angle, but rather on the fact that any branching angle below 90° can lead to the possibility that fundamentally different network architectures satisfy the simultaneous requirements of forward growth and side branching. Our model focuses on the geometrical aspects of this situation (in particular filament orientation and obstacle shape). In the future, it might be extended by other important aspects of this complex biological system, including the details of the filament–membrane interaction and the role of filament bending [20, 38].

In general, all our results were benchmarked against stochastic computer simulations which in principle can be used to include many details of the underlying molecular processes. Here we have adopted the established view that polymerization, branching and capping are the dominating processes in the context of growing actin gels. For relatively simple linear

obstacle shapes, a rate equation (ODE) model yielded accurate results and, due to its reduced complexity, also allowed for analytical progress. Using this approach, we found that either of two competing orientation patterns emerges in steady state and transitions between the two are triggered mostly by changes in the velocity of the obstacle. A similar result has already been obtained in earlier studies for a flat obstacle with large lateral extension, where filament orientation distributions with characteristic peaks at either $+70/0/-70$ or ±35 have been found to dominate the steady state of growing networks [31, 32]. These results were now extended to finite sized obstacles. We find that for very small objects, the $+70/0/-70$ pattern is dominant, while for larger objects, mutual stability of the two patterns recovers. In case of obstacles with a tilted straight contour (linear obstacles), again very similar patterns are predicted. However, for most parameter configurations they have to be interpreted within a rotated obstacle frame.

Curved (nonlinear) obstacle shapes have been analyzed in the ODE-model using a piecewise-linear approximation of the given geometry. As an alternative, a continuous spatial coordinate in the horizontal direction was introduced to the model equation by incorporating a filament advection term, thus yielding a PDE-model. The additional benefit of this spatial resolution clearly lies in the gain of accuracy compared to results obtained earlier. For specific parameter combinations, it was shown that the lack of spatial resolution can lead to incorrect predictions regarding the resulting filament patterns in steady state. Analysis of nonlinear obstacle shapes in the PDE-model yielded an apparent coexistence of the two competing network patterns at different horizontal positions along the obstacle surface in the lab frame. A transformation to the obstacle frame, locally at each lateral position, however revealed that one unique orientation pattern is dominating the network structure as before. Again, these results are in good agreement with computer simulations.

In order to experimentally test these theoretical predictions, the method of choice would be electron tomography [22, 24, 26], although in the future super-resolution microscopy like dual-objective STORM might become an interesting alternative [50]. In the context of a rapidly increasing image quality of EM data for actin networks, the correct analysis and interpretation of the measured observables becomes increasingly important. Therefore, a detailed understanding of the structural network characteristics emerging under different situations is indispensable. In this work, we have also shown that the extracted orientation distribution of actin filament networks from experimental EM images growing at the surface of non-uniform obstacles can be easily misinterpreted. We have shown that a standard measurement in the lab frame would yield apparently novel patterns that could not be explained by existing models. For a correct interpretation of such findings, we introduced a rotated obstacle frame which lies locally orthogonal to the obstacle surface. Within this reference frame, the seemingly novel filament orientation patterns are rationalized and can be understood in terms of the two well known filament distributions, peaked at $+70/0/-70$ or ±35. Thus our results also contribute to improving the way experimental data can be compared to theoretical predictions.

A convenient setup to test our predictions would be the combination of electron tomography with biomimetic assays with particles of various shapes, which earlier have been analyzed mainly in regard to macroscopic variables such as propulsion velocity and shape of the comet tail [11]. Apart from obstacle shape, the obstacle velocity relative to the filament polymerization speed is a central parameter in the model which triggers transitions between filament orientation patterns. This velocity could be adjusted for instance by applying a force against network growth diminishing steady state growth. Changing the biochemical reaction rates for capping and branching is expected to be of minor importance and could be tested by

IOP Institute of Physics 🔶 DEUTSCHE PHYSIKALISCHE GESELLSCHAFT

varying the concentration of purified protein solutions in the assay. As an additional benefit of introducing different obstacle geometries in experiment, this might also lead to a deeper understanding of Arp2/3 activation close to the surface of the obstacle, which is one of the most important questions still to be clarified in the context of actin-driven motility.

Acknowledgments

References

[1] Carlier M F (ed) 2010 *Actin-Based Motility* (Dordrecht: Springer)
[2] Mullins R D, Heuser J A and Pollard T D 1998 The interaction of Arp2/3 complex with actin: nucleation, high affinity pointed end capping and formation of branching networks of filaments *Proc. Natl Acad. Sci. USA* **95** 6181–6
[3] Pollard T D 2007 Regulation of actin filament assembly by Arp2/3 complex and formins *Annu. Rev. Biophys. Biomol. Struct.* **36** 451–77
[4] Frischknecht F and Way M 2001 Surfing pathogens and the lessons learned for actin polymerization *Trends Cell Biol.* **11** 30–8
[5] Gouin E, Welch M D and Cossart P 2005 Actin-based motility of intracellular pathogens *Curr. Opin. Microbiol.* **8** 35–45
[6] Lambrechts A, Gevaert K, Cossart P, Vandekerckhove J and Van Troys M 2008 Listeria comet tails: the actin-based motility machinery at work *Trends Cell Biol.* **18** 220–7
[7] Loisel T P, Boujemaa R, Pantaloni D and Carlier M F 1999 Reconstitution of actin-based motility of Listeria and Shigella using pure proteins *Nature* **401** 613–6
[8] Cameron L A, Footer M J, Van Oudenaarden A and Theriot J A 1999 Motility of ActA protein-coated microspheres driven by actin polymerization *Proc. Natl Acad. Sci. USA* **96** 4908–13
[9] Upadhyaya A, Chabot J R, Andreeva A, Samadani A and van Oudenaarden A 2003 Probing polymerization forces by using actin-propelled lipid vesicles *Proc. Natl Acad. Sci. USA* **100** 4521–6
[10] Giardini P A, Fletcher D A and Theriot J A 2003 Compression forces generated by actin comet tails on lipid vesicles *Proc. Natl Acad. Sci. USA* **100** 6493–8
[11] Schwartz I M, Ehrenberg M, Bindschadler M and McGrath J L 2004 The role of substrate curvature in actin-based pushing forces *Curr. Biol.* **14** 1094–8
[12] Boukellal H, Campás O, Joanny J F, Prost J and Sykes C 2004 Soft listeria: actin-based propulsion of liquid drops *Phys. Rev.* E **69** 061906
[13] Beltzner C C and Pollard T D 2008 Pathway of actin filament branch formation by Arp2/3 complex *J. Biol. Chem.* **283** 7135–44
[14] Wiesner S, Helfer E, Didry D, Ducouret G, Lafuma F, Carlier M F and Pantaloni D 2003 A biomimetic motility assay provides insight into the mechanism of actin-based motility *J. Cell Biol.* **160** 387–98
[15] McGrath J L, Eungdamrong N J, Fisher C I, Peng F, Mahadevan L, Mitchison T J and Kuo S C 2003 The force–velocity relationship for the actin-based motility of *Listeria monocytogenes Curr. Biol.* **13** 329–32
[16] Marcy Y, Prost J, Carlier M F and Sykes C 2004 Forces generated during actin-based propulsion: a direct measurement by micromanipulation *Proc. Natl Acad. Sci. USA* **101** 5992–7
[17] Parekh S H, Chaudhuri O, Theriot J A and Fletcher D A 2005 Loading history determines the velocity of actin-network growth *Nature Cell Biol.* **7** 1219–23

[18] Prass M, Jacobson K, Mogilner A and Radmacher M 2006 Direct measurement of the lamellipodial protrusive force in a migrating cell *J. Cell Biol.* **174** 767–72

[19] Heinemann F, Doschke H and Radmacher M 2011 Keratocyte lamellipodial protrusion is characterized by a concave force–velocity relation *Biophys. J.* **100** 1420–7

[20] Zimmermann J, Brunner C, Enculescu M, Goegler M, Ehrlicher A, Käs J and Falcke M 2012 Actin filament elasticity and retrograde flow shape the force–velocity relation of motile cells *Biophys. J.* **102** 287–95

[21] Resch G P, Urban E and Jacob S 2010 The actin cytoskeleton in whole mount preparations and sections *Methods Cell Biol.* **96** 529–64

[22] Vinzenz M *et al* 2012 Actin branching in the initiation and maintenance of lamellipodia *J. Cell Sci.* **125** 2775–85

[23] Svitkina T M and Borisy G G 1999 Arp2/3 complex and actin depolymerizing factor/cofilin in dendritic organization and treadmilling of actin filament array in lamellipodia *J. Cell Biol.* **145** 1009–26

[24] Urban E, Jacob S, Nemethova M, Resch G P and Small J V 2010 Electron tomography reveals unbranched networks of actin filaments in lamellipodia *Nature Cell Biol.* **12** 429–35

[25] Koestler S A, Auinger S, Vinzenz M, Rottner K and Small J V 2008 Differentially oriented populations of actin filaments generated in lamellipodia collaborate in pushing and pausing at the cell front *Nature Cell Biol.* **10** 306–13

[26] Weichsel J, Urban E, Small J V and Schwarz U S 2012 Reconstructing the orientation distribution of actin filaments in the lamellipodium of migrating keratocytes from electron microscopy tomography data *Cytometry* A **81A** 496–507

[27] Carlsson A E and Mogilner A 2010 Mathematical and physical modeling of actin dynamics in motile cells *Actin-Based Motility* ed M F Carlier (Berlin: Springer) pp 381–412

[28] Mogilner A and Oster G 1996 Cell motility driven by actin polymerization *Biophys. J.* **71** 3030–45

[29] Mogilner A and Oster G 2003 Force generation by actin polymerization: II. The elastic ratchet and tethered filaments *Biophys. J.* **84** 1591–605

[30] Carlsson A E 2003 Growth velocities of branched actin networks *Biophys. J.* **84** 2907–18

[31] Maly I V and Borisy G G 2001 Self-organization of a propulsive actin network as an evolutionary process *Proc. Natl Acad. Sci. USA* **98** 11324–9

[32] Weichsel J and Schwarz U S 2010 Two competing orientation patterns explain experimentally observed anomalies in growing actin networks *Proc. Natl Acad. Sci. USA* **107** 6304–9

[33] Schaus T E and Borisy G G 2008 Performance of a population of independent filaments in lamellipodial protrusion *Biophys. J.* **95** 1393–411

[34] Lee K C and Liu A J 2009 Force–velocity relation for actin-polymerization-driven motility from Brownian dynamics simulations *Biophys. J.* **97** 1295–304

[35] Alberts J B and Odell G M 2004 *In silico* reconstitution of Listeria propulsion exhibits nano-saltation *PLoS Biol.* **2** e412

[36] Schreiber C H, Stewart M and Duke T 2010 Simulation of cell motility that reproduces the force–velocity relationship *Proc. Natl Acad. Sci. USA* **107** 9141–6

[37] Gerbal F, Chaikin P, Rabin Y and Prost J 2000 An elastic analysis of *Listeria monocytogenes* propulsion *Biophys. J.* **79** 2259–75

[38] Zhu J and Mogilner A 2012 Mesoscopic model of actin-based propulsion *PLoS Comput. Biol.* **8** e1002764

[39] Verkhovsky A B, Chaga O Y, Schaub S, Svitkina T M, Meister J J and Borisy G G 2003 Orientational order of the lamellipodial actin network as demonstrated in living motile cells *Mol. Biol. Cell* **14** 4667–75

[40] Schaub S, Meister J J and Verkhovsky A B 2007 Analysis of actin filament network organization in lamellipodia by comparing experimental and simulated images *J. Cell Sci.* **120** 1491–500

[41] Ydenberg C A, Smith B A, Breitsprecher D, Gelles J and Goode B L 2011 Cease-fire at the leading edge: new perspectives on actin filament branching, debranching and cross-linking *Cytoskeleton* **68** 596–602

[42] Ti S-C, Jurgenson C T, Nolen B J and Pollard T D 2011 Structural and biochemical characterization of two binding sites for nucleation-promoting factor WASP-VCA on Arp2/3 complex *Proc. Natl Acad. Sci. USA* **108** E463–71

[43] Xu X P, Rouiller I, Slaughter B D, Egile C, Kim E, Unruh J R, Fan X, Pollard T D, Li R, Hanein D and Volkmann N 2012 Three-dimensional reconstructions of Arp2/3 complex with bound nucleation promoting factors *EMBO J.* **31** 236–47

[44] Schafer D A, Jennings P B and Cooper J A 1996 Dynamics of capping protein and actin assembly in vitro: uncapping barbed ends by polyphosphoinositides *J. Cell Biol.* **135** 169–79

[45] Käs J, Strey H and Sackmann E 1994 Direct imaging of reptation for semiflexible actin filaments *Nature* **368** 226–9

[46] Dichtl M A and Sackmann E 1999 Colloidal probe study of short time local and long time reptational motion of semiflexible macromolecules in entangled networks *New J. Phys.* **1** 18

[47] Pollard T D, Blanchoin L and Mullins R D 2000 Molecular mechanism controlling actin filament dynamics in nonmuscle cells *Annu. Rev. Biophys. Biomol. Struct.* **29** 545–76

[48] Weichsel J and Schwarz U S 2012 Unifying autocatalytic and zeroth order branching models for growing actin networks arXiv:1207.4574

[49] Press W H, Teukolsky S A, Vetterling W T and Flannery B P 1992 *Numerical recipes in C: the art of scientific computing* (Cambridge: Cambridge University Press)

[50] Xu K, Babcock H P and Zhuang X 2012 Dual-objective STORM reveals three-dimensional filament organization in the actin cytoskeleton *Nature Methods* **2** 185–8